World Scientific
www.worldscientific.com

Ground semi-physical simulation experiment study of one-dimensional drag-free control

Chu Zhang[*], Jianwu He[*], Mingwei Chen[*,†], Li Duan[*,†] and Qi Kang[*,†,‡]

[*]National Micro Gravity Laboratory, Institute of Mechanics, CAS, Beijing 100190, China

[†]School of Engineering Sciences, University of Chinese Academy of Science,
Beijing 100049, China

[‡]kq@imech.ac.cn

[§]On behalf of The Taiji Scientific Collaboration

Drag-free control is one of the key technologies for the verification of Taiji-1 satellite. In the direction of sensitive axis, the drag-free controller receives the measurement signal from the high-precision gravitational reference sensor on the satellite, and instructs the micro-thruster system to counteract the disturbance force acting on the sensitive axis, so that the microgravity level in the sensing axis direction of the satellite can reach the order of 10^{-9} m/s^2 in the measurement band. In order to fully verify the drag-free control system, a ground one-dimensional drag-free semi-physical simulation system is built to simulate the performance of various payloads in the drag-free control loop, and to verify the performance and technical targets that the drag-free control system can achieve in the ground control loop. Through the small angle approximation, the equivalent relationship between the rotation of the experimental model and the translational motion of the experimental satellite in the direction of drag-free is demonstrated. In the condition of neglecting the stiffness and damping of the suspended pendulum, the parameters of the suspended pendulum are designed according to the principle of equal acceleration, and their effectiveness is verified by numerical simulation. According to the operation mode of on orbit drag-free control, the ground drag-free experimental scheme and drag-free controller are designed, and the experimental research and verification are carried out. The results show that the controller can effectively control the displacement and acceleration of the experimental model, and also can effectively suppress the disturbance of certain amplitude and frequency.

Keywords: Drag-free control; acceleration equivalence; suspended rotational pendulum; displacement mode.

[‡]Corresponding author.
[§]For more details, please refer to article 2102002 of this Special Issue.

1. Introduction

Drag-free satellites have important applications in satellite navigation,[1] earth gravity field measurement,[2] space general relativity verification[3] and gravitational wave detection.[4] Drag-free satellites with high precision gravitational reference sensor are able to measure the acceleration of satellites or the displacement between the satellite and test mass. The drag-free controller receives the measurement information, orders the micro-thrust system to counteract the nonconservative force on the satellite body, and makes the satellite body and the test masses reach a very high microgravity level, which provides conditions for various space science experiments. In space gravitational wave detection, the test mass inside the satellite, served as the inertial reference frame for inter-satellite laser interference, must maintain its own residual acceleration at a very low order of magnitude, about 10^{-15} m/s^2@10^{-3} Hz.[5] This technical requirements brings a great challenge to drag-free satellite control system. European Space Agency, Chinese Academy of Sciences and other research institutions have successively launched drag-free technology verification satellites to certify related technologies about drag-free control system.

In view of the important applications of drag-free satellites and missions proposed by national space agencies, researchers were devoted to the extensive numerical simulation studies on drag-free satellite control system. The embedded model control theory, proposed by Donati and Vallauri in 1984, was developed and applied to the accelerometer mode drag-free control system of gravity field measurement satellites in low Earth orbit by Canuto.[6] Drag-free satellites for gravitational wave detection has always been a hot topic in the field of drag-free control. The reasons are as follows: on the one hand, it can contain a variety of configuration structures for the test mass, such as single test mass,[7] collinear two test masses[8] and two test masses at an angle of 60°[9]; on the other hand, the performance requirements of drag-free satellite for gravitational wave detection are much higher than other drag-free satellites.

Many researchers have studied the problem of drag-free control for gravitational wave detection satellites. They decouple the coupling between different degrees of freedom of the internal test masses of the satellite through the feedback connection of the whole drag-free system, so that the multi-degree of freedom drag-free system is decoupled into a series of single input single output systems, and the controller of single input single output loop is designed by various control synthesis methods, including the PID controller,[10] the optimization controller based on the weight function,[11] $\mathcal{H}_\infty$ controller.[12] Through the numerical simulation for LISA Pathfinder drag-free control system, the controller with quantitative feedback was designed by Wu *et al.*,[13] who studied the tracking performance of displacement drag-free mode under the failure of a single thruster. But in all of these studies, the structural uncertainty of the dynamic system of test mass is not considered. Thus, a new design method of robust controller was proposed by Pettazzi,[14] utilizing the ν-gap metric to simplify and decouple the uncertain drag-free system and designing the controller of the decoupled system based on the singular value of the mixed structure. However, this decoupling method is

approximate so that the extra error would generates. Besides, this method of designing controller is so complex and the order of the controller is so large as to complete it hardly. In addition, the usual robust controllers are relatively conservative, to some extent, resulting in sacrifice of the control performance.

The research on drag-free control not only includes controller design and numerical simulation, but also adopts the ground hardware in the loop simulation method to study drag-free control system. For example, in the 1960s, Stanford University led the development of GP-B satellite and carried out ground simulation experimental research.[15] In the 1980s, Japanese scientists began to carry out ground experiment simulation of drag control.[16] Compared with the ground semi-physical simulation of traditional satellite, the ground semi-physical simulation of drag-free satellite exists some specific difficulties. The first one is to build the ground experimental platform that must be capable of emulating the high level of microgravity in the satellite. In addition, the device built on the ground should be able to simulate the space-borne high-precision gravitational reference sensor, which generally ranges from 10^{-4} to 10^{-6} m/s^2. Third, it is the micro-thrust system mounted on the satellite that needs to be imitated on the ground to counteract the disturbing force of the satellite body for tracking the test mass under the displacement mode of drag-free control. All of the above difficulties have restricted the development of ground emulation of drag-free control. Therefore, the ground test of drag-free control system focuses more on the ground verification of single system, including high-precision gravitational reference sensor and micro-thrust system.

The suspended torsion pendulum plays an important role in the ground test of GRS and micro-thruster system, because its high sensitivity. The sensitivity, noise model and cross-coupling between different degrees of freedom of the high-precision GRS could be tested by the suspended rotational pendulum at The University of Trento, Italy.[17] Huazhong University of Science and Technology applied the suspended rotational pendulum not only into the analogous test for high precision GRS,[18] but also into the measurement of the thrust of micro-thruster[19] and the universal gravitation constant.[20] Based on the high sensitivity of the suspended rotation pendulum in the direction of spin, it can be explored that the pendulum is equivalent to the satellite to design the ground simulation experimental of drag-free control system.

In this paper, a semi-physical simulation system of drag-free system is built on the ground. On the basis of fully understanding the working principle of drag-free satellite, the translational motion of the Taiji-1 satellite along the drag-free control sensitive axis is equivalent to the rotation of the ground torsion pendulum according to the principle of dynamics and main physical quantities equivalent. On this basis, a drag-free suspension pendulum is designed to build the semi-physical simulation system, and the ground drag-free working modes corresponding to different operating modes on the satellite and the corresponding drag-free controller are designed to verify the functions and technical specifications of the drag-free system. This paper is mainly divided into the following parts: the first part is the introduction, the second part is the experimental device and its

design, the third part is the experiment and result analysis of drag-free control, and the fourth part is the conclusion.

2. The Designs of Experimental Devices

The Taiji-1 satellite operates in an orbit about 600 km above the ground. In the radial direction along the orbit, where the experiment of drag-free control would be carried out, the nonconservative force applied on the satellite is less than 1 μN. Two groups of micro-thrusters ought to, respectively, be mounted on two sides of this direction of the satellite, as shown in the left in Fig. 1. In the process of drag-free system experiments, a set of micro-thrusters actively exert the sine disturbing force on the controlled object, ranging from 10 to 100 μN amplitude range. It is the acceleration or displacement signal produced by the GRS that can be received by the drag-free controller, which generates real time control command to the other side micro-thrusters to counteract the effects of disturbances.

The suspension torsion pendulum can be taken as a counterpart of the satellite, as shown in Fig. 1. The torsion stiffness of the suspension wire is so small that the translation of the satellite along the drag-free control direction, in the case of small angle rotation, could be approximately equivalent to the rotation of the pendulum. The disturbance force acting on the pendulum, the corresponding position of the pendulum where electrostatic combs are installed would induces acceleration. A displacement sensor needs to be placed at the far end of the pendulum to measure the displacement of the corresponding position, received by the drag-free controller which control the micro-thrusters to counteract the disturbance. It is the thought of experiments that simulates single-axis drag-free control on the satellite.
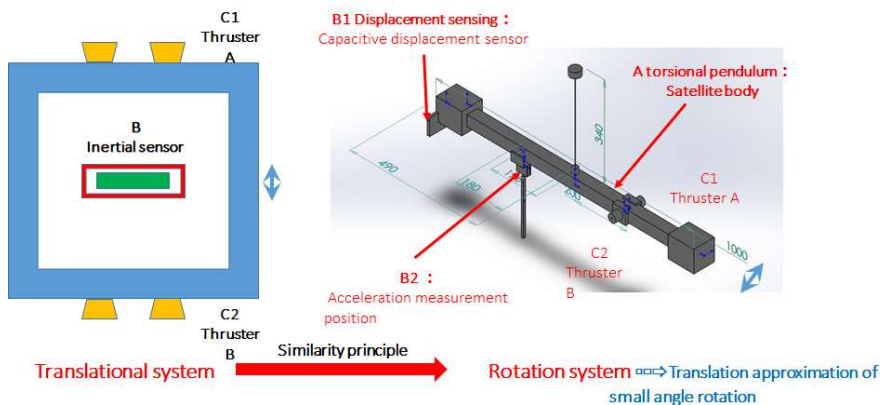

Fig. 1. Schematic diagram of drag-free semi-physical simulation experiment.

2.1. *The experimental model of ground drag-free control*

Through the small angle approximation, the torsional dynamics of the suspension pendulum of the ground experimental model is equivalent to the dynamics of the experimental satellite drag-free control direction. Given that the stiffness and damping of the suspended pendulum are so small as to be omitted, the model parameters of the pendulum are obtained on the basis of the principle of equal acceleration. Then according to objective conditions as well as the approximate equivalent relationship between the experimental model and the experimental satellite, the parameters of the model are preliminarily selected, which must be confirmed by numerical simulation. Based on this, a detailed experimental model is ultimately designed.

2.1.1. *The principle of equal acceleration*

Without regard to the influence of stiffness and damping, the dynamics model of the rotational pendulum is as follows:

$$J\alpha = M, \tag{1}$$

where J is the moment of inertia, α is the angular acceleration of the pendulum around the fulcrum. The moment applied on the pendulum is as follows:

$$M = F_d L_1, \tag{2}$$

where F_d is the disturbing force exerted on the pendulum. L_1 is the arm of disturbance force. The acceleration of the position the sensor measured is as follows:

$$a = L_2 \alpha, \tag{3}$$

where L_2 is the distance between the sensor and the center of the pendulum. Formula (2), (3) and (4) can be incorporated as follows:

$$a = L_2 \frac{M}{J} = \frac{F_d L_1 L_2}{J} = \frac{F_d}{\frac{J}{L_1 L_2}}. \tag{4}$$

The equivalent mass of the pendulum is m. Therefore, the following equation could be deduced:

$$m = \frac{J}{L_1 L_2}. \tag{5}$$

The dynamics model of the satellite in the direction of drag-free control is

$$F_s = m_s a_s, \tag{6}$$

where m_s is the mass of the satellite. The disturbance force acting on the satellite is F_s. Supposed that the acceleration caused by the disturbance exerted on the satellite is equal to one on the pendulum, the relation between the dynamic parameters of the satellite and the pendulum could be established as follows:

$$a = \frac{F_d}{\frac{J}{L_1 L_2}} = a_s = \frac{F_s}{m_s}. \tag{7}$$

Table 1. Designs of the pendulum and thrusters.

Code of design	The controlled objects	Mass (kg)	Designs of thruster	Acceleration range
			Equal acceleration	
Scheme 0	The microgravity technique experimental satellite m_s	180	Two thrusters Range from 10 to 100 μN	5.5×10^{-8}~5.5×10^{-7} m/s^2
Scheme 1		90	Single thruster Range from 5 to 50 μN	
Scheme 2A	The rotational pendulum m	18	Single thruster Range from 1 to 10 μN	
			Equal thrust force	
Scheme 2B			Single thruster Range from 10 to 100 μN	5.5×10^{-7}~5.5×10^{-6} m/s^2

The mass of the satellite in orbit is about 180 kg. In accordance with above all deduction and formulas, several designs of the suspended pendulum are determined.

As shown in Table 1, Scheme 0 has been applied to the test of experimental satellite on orbit, the disturbing force affecting on one side of the satellite ranges from 10 to 100 μN, the homologous acceleration ranging from 5.5×10^{-8}~5.5×10^{-7} m/s^2. Scheme 1 and Scheme 2A designed based on the principle of equal acceleration, the equivalent mass of suspension pendulum is 90 kg and thrust force produced by single thruster is between 5 and 50 μN. Different with Scheme 1, in Scheme 2A, the mass is 18 kg and the thrust ranges from 1 to 10 N. According to the principle of thrust equality, the acceleration at the measurement position in Scheme 2B varies in proportion with range of thrust in Scheme 2A.

According to Eq. (7), the rotational inertia of the pendulum is dependent on the equivalent mass, which is 3.6 kg·m^2 in Scheme 1, while it is 0.72 kg·m^2 in Scheme 2A and Scheme 2B. Consequently, the mass must be taken into account as well as the size of the pendulum which is confined to the size of vacuum tank (diameter is 800 mm and length is 1200 mm). The one reason is that the vacuum tank provides a vacuum environment where the ground experiment shall be carried out. The other reason is that, in case the wire broke, the gravity of the pendulum must be less than the yield limit of tungsten fiber. So, Scheme 2 is decided as the final choice. The specific design of the model, including mass, size and other correlative parameters, will be referred to in Sec. 2.1.3.

2.1.2. *The validation of approximate principle by numerical simulation*

Formula (7) is obtained at the condition of ignoring torsion stiffness and damping. Hence, the dynamics similarity relationship between the experimental model and experimental satellite in the direction of the drag-free control must be verified by numerical simulation. The model is suspended by the tungsten fiber. Its diameter is about 300 μm and length is about 340 mm. The calculation formula of the torsional rigidity is as follows:

$$k = \frac{\pi(d/2)^4 G}{2l},$$

(8)

Table 2. Parameters of the tungsten fiber.

Length	$l = 340$ mm
Diameter	$d = 0.3$ mm
The elastic modulus and Poisson's ratio	$E = 410$ Gpa, $\sigma = 0.3$

where G is the shear modulus of tungsten fiber.

$$E = 2(1 + \sigma)G, \tag{9}$$

where E is the Young's modulus of tungsten fiber. The values of every parameter are shown in Table 2.

Substitute the above values into the formulas (8) and (9). Then k is calculated as follows:

$$k = 8.3 \times 10^{-5} \text{N} \cdot \text{m/rad}.$$

The damping of the suspended pendulum is negligibly small. At the same time, the torsional rigidity is in the order of 10^{-5} N·m/rad. Therefore, the dynamic model could be built.

$$J\ddot{\theta} + k\theta = M = F_d L_1. \tag{10}$$

The rotational inertial of the pendulum is taken by 3.5 kg·m². The value of disturbing force arm is 0.2 m. In addition, the disturbing force is modeled as follows:

$$F_d = \big(30 + 10 \sin(2\pi \times 0.05t)\big)/2 \, \mu\text{N},$$

where F_d applied on the pendulum without the active control force exerted on it, the angle acceleration could be acquired. And then the value of L_2 is taken as 0.2 m, the acceleration of measuring point can be calculated, as shown in Fig. 2(a). The displacement of the torsion pendulum and the displacement of the acceleration measuring point are as shown in Fig. 2(b).

The motion period of the model is about 1293.6 s. When the damping and stiffness coefficients are extremely small, the model can effectively simulate the external acceleration of the satellite within the first 100 s. During the process of orbiting, the drag-free control frequency of satellite is 4 Hz. Figure 2(b) shows that the displacement at the measuring end of the displacement sensor is approximately 15 nm and one of the accelerometer is approximately 10 nm, at 0.25 s.

Remaining value of torsion stiffness and the simulation results are shown below when the experimental model J is 0.7 kg·m².

The motion period of the model is about 578.5 s. When the damping and stiffness coefficients are extremely small, the model can effectively simulate the external acceleration of the satellite within the first 50 s. Figure 3 shows that the displacement at the measuring end of the displacement sensor is less than 15 nm and one of the accelerometer is less than 10 nm, at 0.25 s.
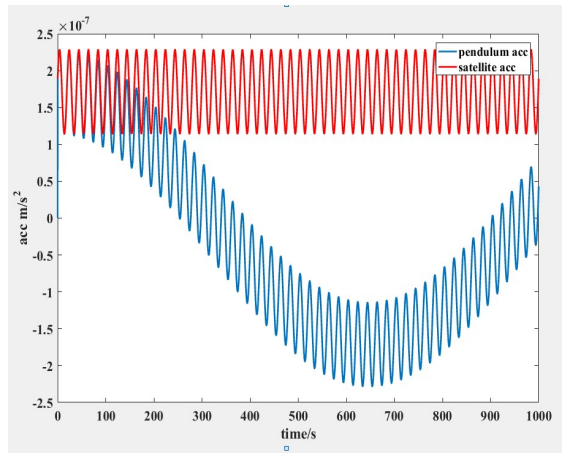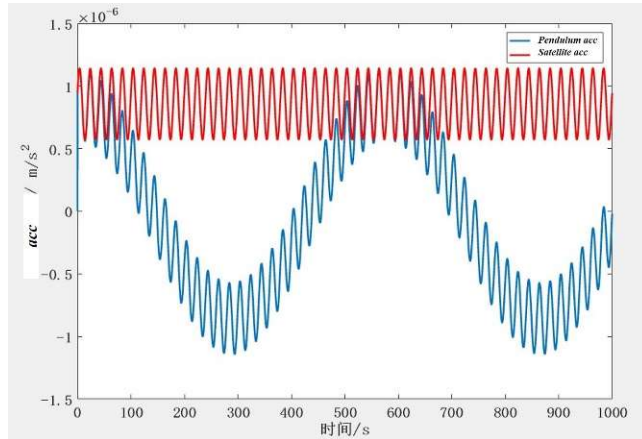
(a)
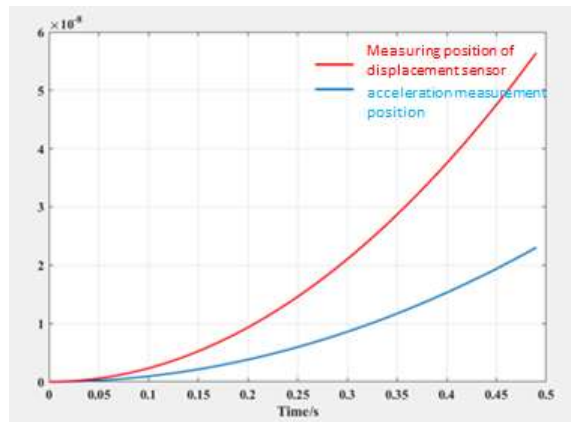
(b)

Fig. 2. (a) Comparison of acceleration and satellite acceleration between torsion pendulum and satellite under the action of disturbing force and (b) comparison of torsion pendulum displacement between displacement sensor and acceleration measurement position.

Simulations reveal the following:

(1) Due to the presence of the stiffness of the suspension pendulum, the model can only be equivalent to imitate the motion of the satellite in the initial period of time when it is disturbed;

(2) the greater the rotation inertia of the suspension pendulum, the longer the perturbing time of the suspended pendulum equivalent to the time of satellite in the perturbation and the smaller the displacement that can be measured by the displacement sensor and accelerometer, which puts forward higher requirements for the resolution of the displacement sensor;

(a)
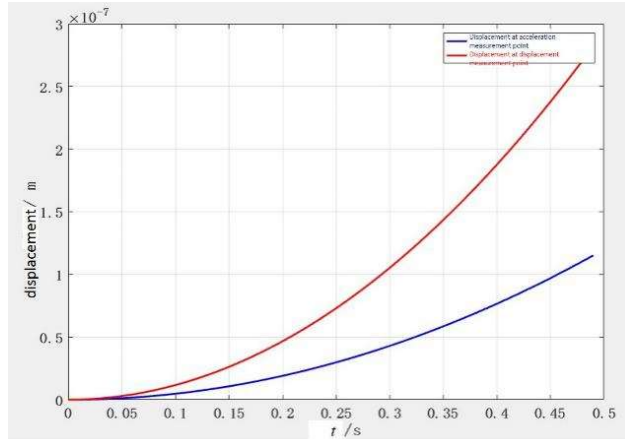
(b)

Fig. 3. (a) Comparison of acceleration and satellite acceleration between torsion pendulum and satellite under the action of disturbing force and (b) comparison of torsion pendulum displacement between displacement sensor and acceleration measurement position.

(3) the stretch strength of suspension wire is the key factor to determine the performance of the pendulum, and then determines the selection of model parameters.

2.1.3. *The experiment model of ground drag-free control*

Based on the analysis in the previous section and considering the environmental constraints of the actual vacuum chamber, the model of the experimental suspension pendulum is determined, including a tungsten wire of length 400 mm, a Yin steel material

Table 3. The related parameters of the suspension rotational pendulum.

Parameters of pendulum	Value
Length of the tungsten fiber	$l = 400$ mm
Length of the pendulum	$L = 600$ mm
Distance between centers of the thruster and the suspension position	$L_1 = 144$ mm
Distance between the capacitance displacement sensor and the center of the suspension position	$L_3 = 200$ mm
Diameter of the tungsten fiber	$r = 0.3$ mm
The elastic modulus and Poisson's ratio of the tungsten fiber	$E = 410$ Gpa, $\sigma = 0.3$
The torsional rigidity of the tungsten fiber	$k = 8.3 \times 10^{-5}$ N·m/rad
The mass of the counterweight	2 kg $\times 4$
The mass of the pendulum	3.6 kg
The rotational inertial of the pendulum	$J = 0.7$ kg·m^2
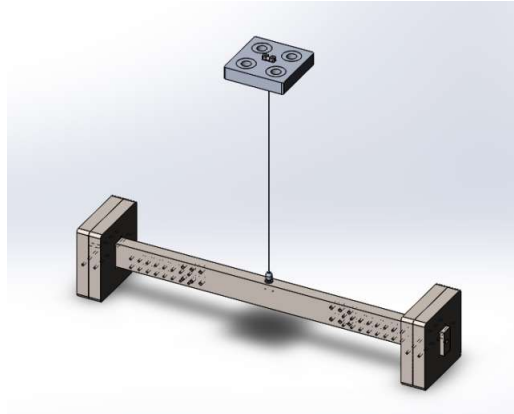
Fig. 4. The model of experimental suspended pendulum.

pendulum of dimension 600 mm × 40 mm × 20 mm and four stainless steel counterweights. The 3D model of experimental suspended pendulum is shown in Fig. 4. Detailed parameters are shown in Table 3.

2.1.4. *The pendulum motion of the suspended pendulum*

The suspension rotation pendulum exists the rotation around the tungsten fiber as well as the single pendulum motion around the upper fulcrum. The pendulum motion comes from two aspects. On the one hand, it comes from the energy in the initial released stage of the pendulum itself. The total weight of the pendulum is about 12 kg, and the damping of the pendulum in the vacuum tank is so small that a long time is taken to dissipate the
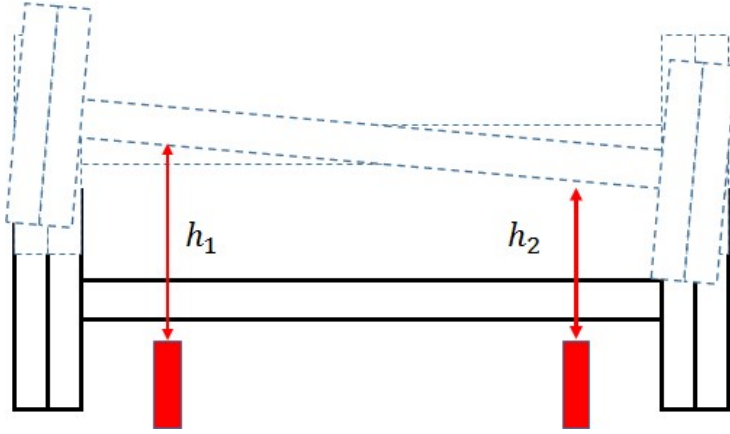
Fig. 5. Differential measurement with double displacement sensors.

energy below the resolution of the displacement sensor. On the other hand, when the active control force and the perturbing force are exerted asymmetrically on the pendulum, the single pendulum motion of the suspended pendulum would be stimulated naturally. Therefore, in order to restrain the influence of pendulum motion on experiment, the scheme of measurement and control are introduced, respectively, into the experiment.

The translational motion will be produced by the disturbing force F_d acting on the pendulum. The deflection displacement caused by the moment M of disturbing force applied on the pendulum cannot be directly measured by using one displacement sensor, so the single pendulum motion model of the torsional pendulum should be defined as follows:

$$F_d l = mgl\varphi. \tag{11}$$

According to the above equation, the formula, $\varphi = F_d/mg$ could be deduced. And m is the total mass of the model about 12 kg. The maximum value of F_d is 100 μN, resulting in the max degree of φ is 850 nrad. And the corresponding displacement is about 300 nm. In consequence, two displacement sensors should be utilized to measure the displacement. Then the difference between two measuring results should be obtained as the displacement, defined as the differential mode displacement induced by the rotation of the pendulum.

As shown in Fig. 5, the design of the measurement devices and the two identical capacitive displacement sensors are placed at the completely symmetrical position. Afterwards, the difference between two measuring results, namely the differential mode displacement, causes that the deflection angle of the pendulum can also be calculated. The formula is as follows:
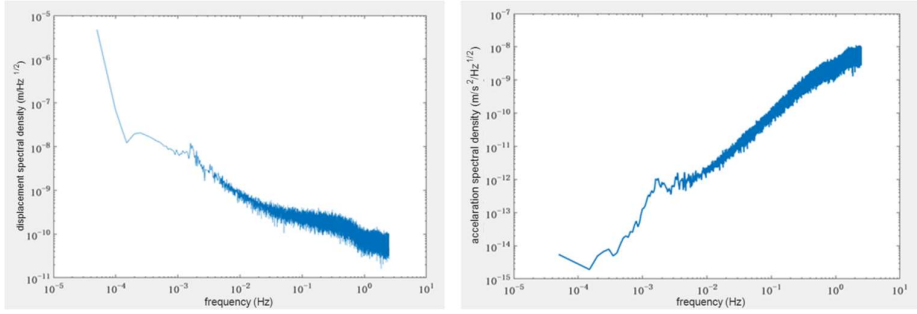
$$\theta = \frac{h_1 - h_2}{2L_3}. \tag{12}$$

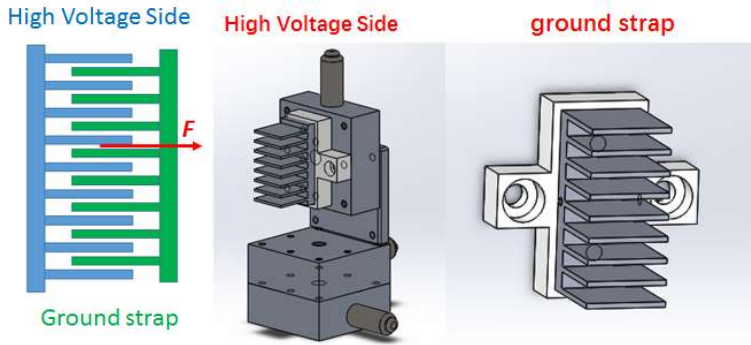Fig. 6. Measurement noise of capacitance displacement sensor.

Fig. 7. Structure diagram of electrostatic comb.

Furthermore, the addition of two measuring results is the common mode displacement

$$\varphi = \frac{h_1 + h_2}{2l}. \tag{13}$$

2.2. *Measurement and control system*

The system also includes sensor system and actuator system. The sensor system adopts the capacitive displacement sensor of type capaNCDT6530 in possession of a cylindrical probe with an inner hole plug, produced by micro-epsilon Company. The sensor has a measuring distance in the range of 0 and 500 μm, the absolute error of value 0.25 μm, the static resolution of value 0.375 nm and the dynamic resolution of value 10 nm. The noise spectrum of the sensor is shown in Fig. 6. The executor applied to the experimental model is an electrostatic comb. Its structure is shown in Fig. 7.

The low voltage end of the electrostatic comb is mounted on and grounded by the pendulum, while the high voltage end is placed on the displacement table so that the vertical distance between the electrostatic comb teeth can be precisely adjusted by the
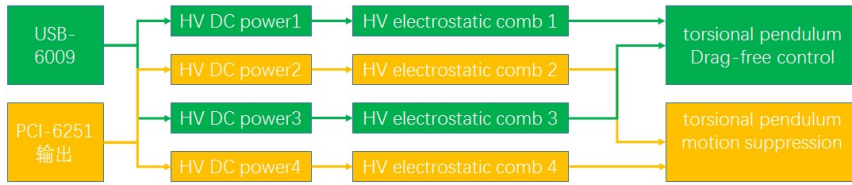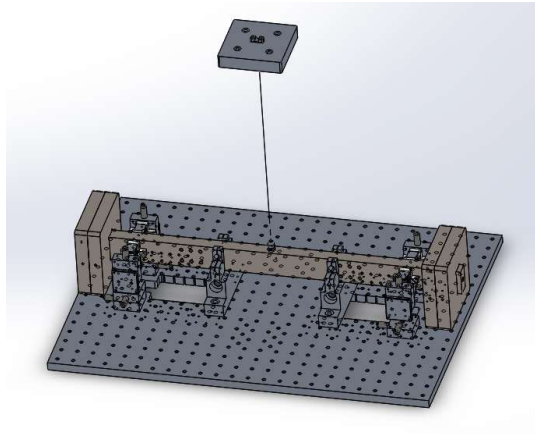
Fig. 8. Distribution of static control force.

Fig. 9. Experimental model of one-dimensional drag free control on the ground.

displacement table. In addition, the high-voltage end is connected to the high-voltage source on the external vacuum through the cable. As shown in Fig. 8, two sets of data acquisition devices and output control equipment from NI Company are used to control the output of the high-voltage power supply to adjust the force among the electrostatic comb teeth in real time. NI USB-6009 and NI PCI-6251, respectively, contain two output terminals, which will generate corresponding voltage ranging from 0 to 5 V in accordance with the control instruction. The voltage induced by these output ends will pass through the high-voltage source as input information, and then a voltage of 0–2000 V will be produced to the high-voltage end of the electrostatic comb tooth according to the linear relationship with the input information. The model of all the above systems assembled as shown in Fig. 9.

The mass of assembled experimental model is 11.5 kg. The center distance between the probe of the two displacement sensors and the suspended tungsten wire is 200 mm. The experimental model consists of four pairs of electrostatic combs, which are installed symmetrically on two sides of two ends of the pendulum. The distance between the electrostatic comb and the center of the tungsten fiber is 144 mm. In the actual adjustment, a rotary displacement table which install the top of the suspension wire on would be capable to regulate the initial position of the pendulum. The length of the tungsten fiber is 400 mm, which deduces that from formula (5), the equivalent mass of

the pendulum is 24.3 kg. The mass of the satellite is 180 kg, so the reduction ratio of mass is 7.4.

3. The Displacement Mode of Drag-Free Control

There are two main working modes of in-orbit drag-free experimental satellite, accelerometer drag-free control mode and displacement drag-free control mode. In the acceleration mode, the controller receives the onboard accelerometer signal and counteracts the nonconservative force affecting on the satellite. In the displacement mode, the inertial sensor measures the displacement of the test mass with respect to the satellite body and thrust would counteract the nonconservative force to make the satellite track the detection mass. The ground experiment mainly verifies the displacement drag-free mode. In this mode, displacement detected the sensor by point input the controller to control the experiment model to close the equilibrium position, thrust counteracting the disturbing force exerted on the suspended pendulum. Measurement points of acceleration could be gained by taking the derivative of the displacement of measuring points, corresponding to the acceleration of the satellite. The ground drag-free simulation mainly includes three working modes, which are, respectively, described in this section.

3.1. *The differential control mode*

Differential control mode means that the deflection angle of the pendulum around the wire acquired by differential mode displacement is taken as the process variables for the displacement drag-free control mode, and its control structure is shown in Fig. 10. Sensor probes 1 and Sensor probes 2 detect the displacement of both ends of the pendulum relative to the equilibrium position. Consequently, the deflection angle is obtained by the calculation of formula (12). As shown in Fig. 11, the reference input of deflection Angle is set to zero. The difference between it and the actual value is considered as the input of the PID controller. The output value of the PID controller is the torque to bring the pendulum back to the balance position. The required thrust, namely the electrostatic comb force. Then the output voltage of the high-voltage power supply is calculated according to the specific relation between the electrostatic comb force and the voltage. The input voltage of the high-voltage source, which is also the output voltage of the control system, could be obtained from the linear relation between the input and output of the high-voltage source. However, these values are in the program and cannot be transmitted as signals. As a result, the data acquisition card is needed to convert the output voltage value of the control system into a signal that can be received by the high-voltage power supply. It should be noted that in the actual experiment, only tension can be generated between the high voltage end and the ground end of the electrostatic comb. In the experiment, four pairs of electrostatic combs are utilized to realize control of the position of the pendulum, including EC1 realizing the clockwise control and EC2 realizing the counterclockwise control. Data acquisition, controller design and output control of the control system are all realized by Labview.
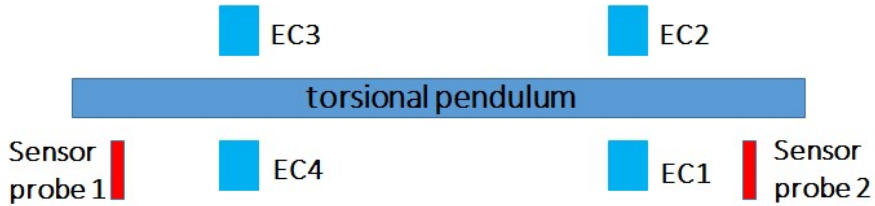
Fig. 10. Configuration diagram of displacement sensor and electrostatic comb.
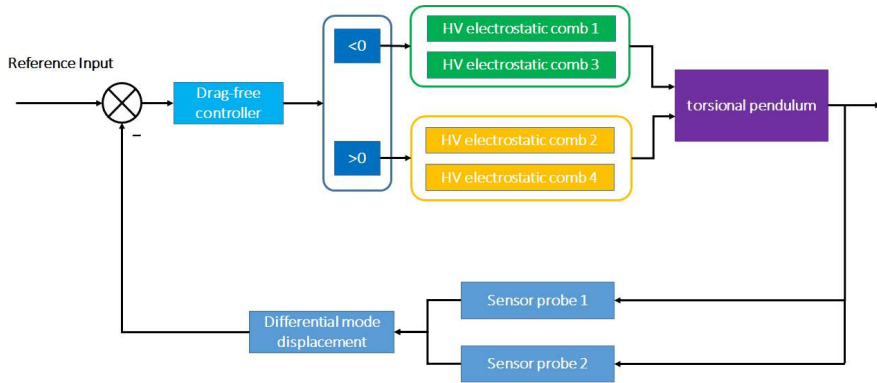

Fig. 11. Displacement drag-free differential mode control.
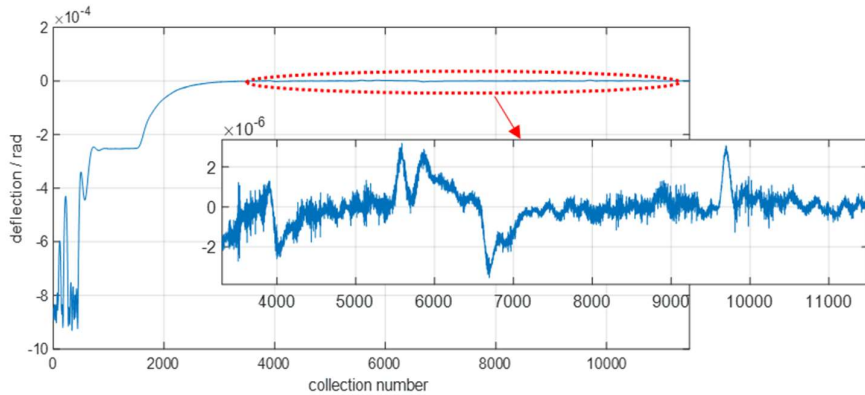

Fig. 12. Deflection angle of torsion pendulum.

The experimental data are obtained by the experiment under the mode of differential mode control. Figure 12 shows the process of the torsion pendulum from the free to the stable state captured by the electrostatic comb control force, and the final deflection angle gradually approaches zero.
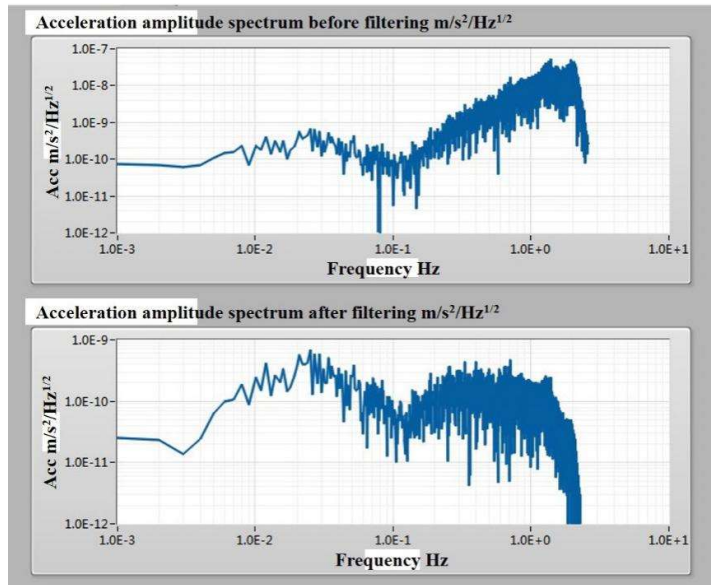
Fig. 13. Acceleration amplitude spectral density at measurement points of torsional pendulum displacement before and after filtering.

The deflection angle of the torsion pendulum can be controlled stably in the order of 10^{-7} rad through the displacement drag-free control. According to the experimental principle, it is necessary to evaluate the acceleration of the torsion pendulum at the measurement point of the displacement sensor, and obtain the acceleration amplitude spectrum density, which corresponds to the residual acceleration noise in the direction of drag-free control on orbit.

Figure 13 shows the spectrum density of acceleration amplitude at the measurement point of torsion pendulum displacement. Figure 13 shows the result of data without filtering. In the frequency band of 0.01~1 Hz, the residual noise of acceleration at the measurement point is less than 10^{-8} m/s², and at 0.01 Hz, the residual acceleration is better than 10^{-9} m/s². The figure below shows the processing result of the data after low-pass filtering, and the cut-off frequency is 0.125 Hz. The main function of the filter is to eliminate the influence of the vibration in other directions of the torsion pendulum on the measuring point, and only retain the movement in the torsion direction. The experimental results show that the residual acceleration is better than 10^{-9} m/s² in the frequency range of 0.01~1 Hz.

3.2. *Common mode suppression of simple pendulum motion*

In Sec. 2.1.4, the suspended torsion pendulum has a single pendulum motion around the upper fulcrum, which will have an impact on the precision of drag-free control. In order
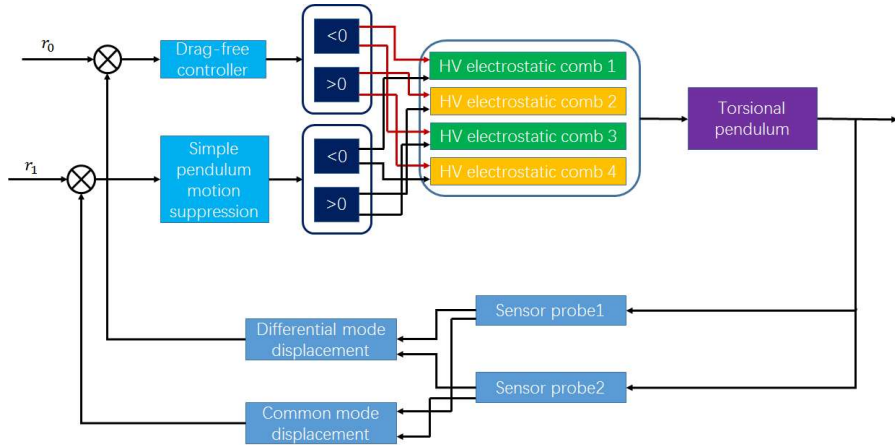
Fig. 14. Differential mode and common mode cooperative control.

to restrain the influence of the pendulum motion on the drag-free control, the common mode cooperative control was applied in this research. The whole process of control is different from the differential mode control in two places, namely, the control variables and the executor. First one is that the common mode displacement was gained by calculating the information measured by two displacement sensors, and then the deflection angle of the pendulum motion, regarded as the control variables, is computed through Eq. (13) as the input of the pendulum motion suppression controller. The output of the controller is the force generated by the electrostatic comb EC1 and EC4 to suppress the single pendulum motion. Acting as a set of actuators, both of them will produce the same tension and inhibit the translational movement of the torsion pendulum away from EC1 and EC4. EC2 and EC3, as another set of actuators, will also induce the same pulling force, preventing the translation away from EC2 and EC3. Note that the cooperative common-mode suppression control runs after the torsion pendulum has entered the stable state of drag-free control. Figure 14 is a block diagram of the coordinated control of torsional pendulum with differential mode drag-free control and common mode single pendulum suppression.

Figure 15 shows the common mode displacement directly obtained from the displacement sensor in the common mode suppression test. Before the common mode suppression control is turned on, the amplitude of the common mode displacement is between 265.1 and 265.3 μm, with obvious periodic motion phenomenon. After the common mode suppression control is turned on, the periodic motion is obviously suppressed. In order to more accurately analyze the change of common mode displacement before and after the control is turned on, the common mode displacement signal is analyzed by spectrum. The results are shown in Fig. 16.
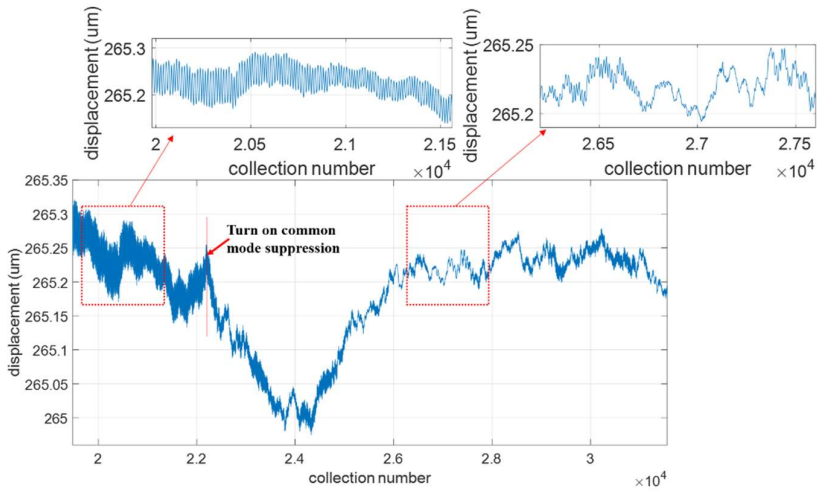
Fig. 15. Common mode displacement of torsion pendulum.
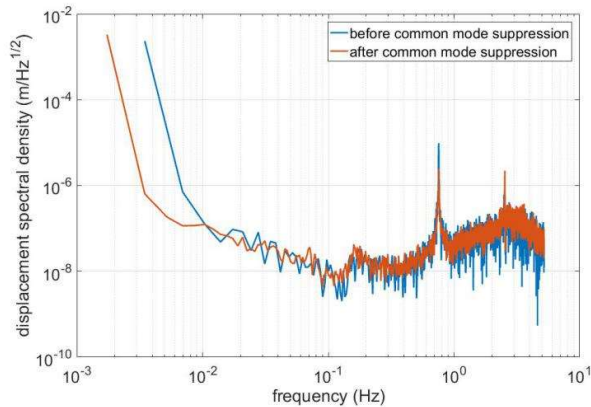

Fig. 16. Displacement amplitude spectral density at measurement points before and after common mode suppression.

As shown in Fig. 16, the amplitude spectrum of common mode displacement before and after common mode suppression is shown. It can be seen from the figure that before the common mode suppression is turned on, the common mode displacement contains two frequency components of 0.76 and 2.5 Hz in the high frequency band, corresponding to the two main vibration frequencies of the suspension torsion pendulum in this direction. After the common mode suppression control is turned on, the vibration mode corresponding to 0.76 Hz main frequency is obviously suppressed, and the vibration mode corresponding to 2.5 Hz main frequency is slightly enlarged. This shows that the

designed common mode rejection controller can effectively suppress the long period motion of the suspended torsion pendulum.

3.3. *Displacement drag-free mode with disturbance*

In the displacement free mode, it is necessary to control the relative absolute reference frame displacement of the ground torsion pendulum or the in orbit experimental satellite into a stable state, and it is also necessary to verify that the torsion pendulum can remain stable under certain disturbance forces. When the drag-free control system runs in displacement mode, one side of the satellite will be perturbed by the perturbation of different frequencies and amplitudes. And then the drag-free controller will send instructions to the micro-thruster on the other side to generate thrust to counteract the disturbing force. In the ground experiment, therefore, the perturbing force is applied on one side of the pendulum while the control system outputs a thrust command received by a thruster at the other side to counteract the disturbance. However, in the natural state, the limiter of the displacement sensor restricts the displacement of the measurement point in the range of 50–450 μm. As a result, in the ground experiment, not until the displacement mode drag-free control operates can the sinusoidal disturbance be applied to the suspension pendulum. Otherwise, the suspension pendulum will encounter the limit device. In this study, after the suspended pendulum became steady firstly by the displacement drag-free mode, one set of electrostatic combs was selected to exert disturbing force with different frequencies and amplitudes, as shown in Fig. 17.

Subsequently, the experiments found that the suspended pendulum would deviate from the balance position at the beginning of changes of the disturbance force and swiftly the drag-free controller would command the other set of electrostatic combs to produce the force to make it return to the balance position. The whole change process of the deflection is shown in Fig. 18.
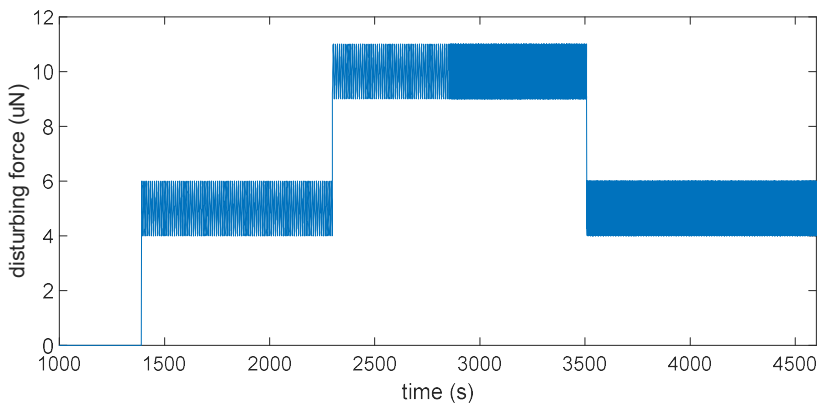

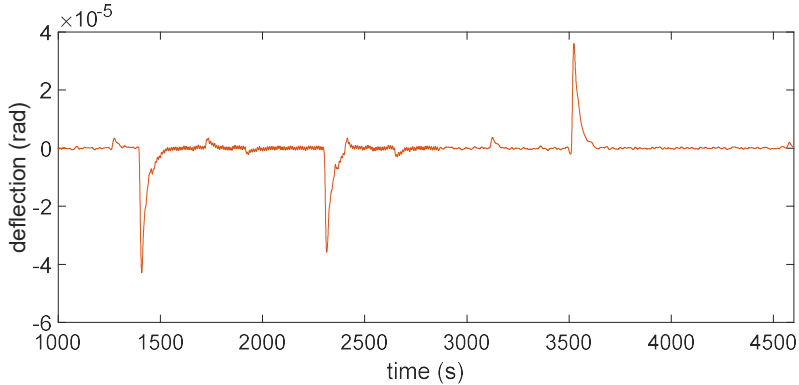Fig. 17. Disturbing force applied to torsion pendulum.

Fig. 18. Variation of deflection angle of torsion pendulum under disturbing force.

It can be seen from Figs. 17 and 18 that the displacement drag-free control can effectively suppress the disturbance force of different frequencies on the torsion pendulum, so that the torsion pendulum can be maintained near the equilibrium position. In order to establish the corresponding relationship with the on orbit drag-free control experiment, two specific schemes are designed to verify the disturbance suppression ability of the displacement drag-free controller. Without considering the difference between the equivalent mass of the torsion pendulum and that of the satellite, the principle of thrust equivalence is adopted to apply the same disturbance force on the torsion pendulum, and the active disturbance force exerted on the satellite is

$$F_{\text{dis}} = 6\sin(2\pi \cdot 0.05 \cdot t) + 30\ \mu N. \tag{14}$$

In order to compare the change of the acceleration at the measurement point of the suspension pendulum before and after the disturbing force is applied, the method of modeling and numerical simulation is used to calculate the acceleration at the measurement point of the torsion pendulum before and after the disturbing force is applied.

Figure 19 shows the monitoring of the acceleration amplitude spectral density at the measurement point of the torsion pendulum during the experiment. The highest peak value in the figure is the response of 0.05 Hz sinusoidal disturbing force on the torsion pendulum.

Figure 20 contains two parts. The red spectrum curve is the displacement amplitude spectrum at the measuring point of the torsion pendulum under the disturbance force of equation (14). The highest peak value is the response of the disturbance force on the torsional mode of the torsion pendulum, and the secondary peak value is the response of the disturbance force on the torsional pendulum. Under the action of displacement drag-free controller, the acceleration of excitation at 0.05 Hz decreases from 10^{-5} to
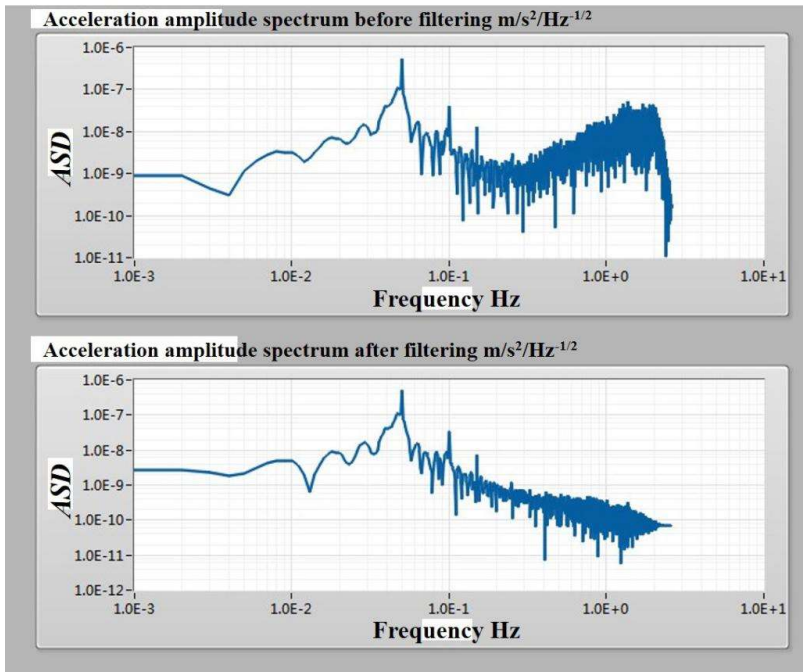
Fig. 19. Real time monitoring value of acceleration amplitude spectrum at measurement point under disturbance.
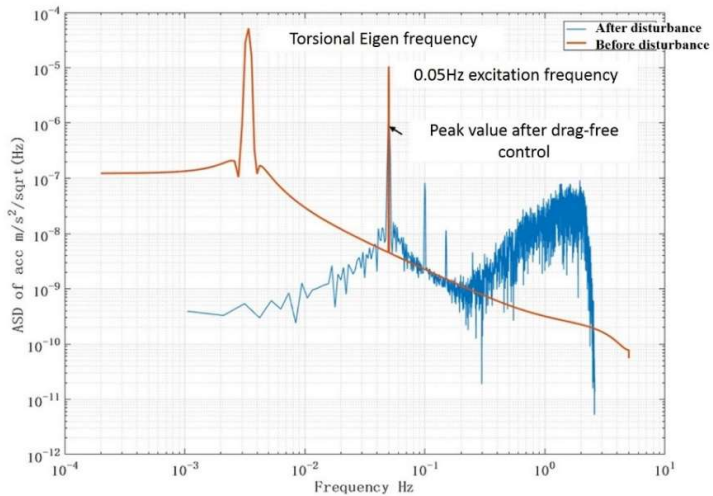

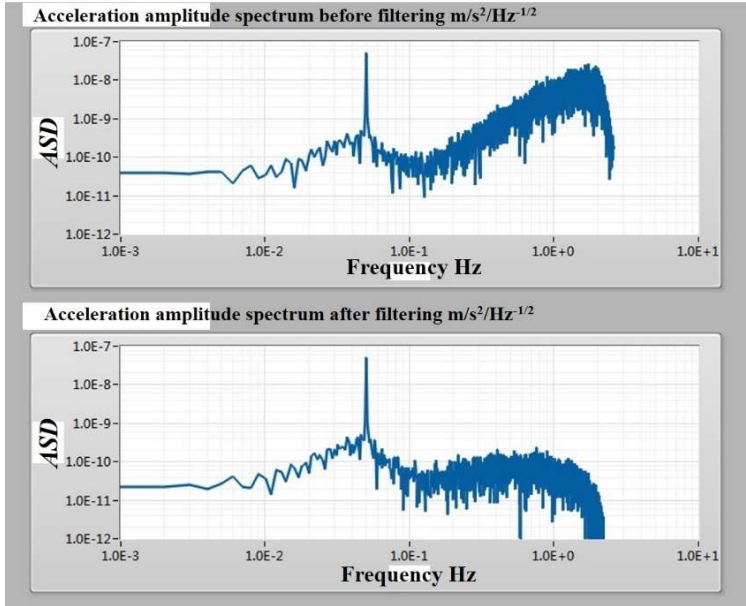Fig. 20. Comparison of acceleration amplitude at measurement point of torsion pendulum before and after disturbance.

Fig. 21. Real time monitoring value of acceleration amplitude spectrum at measurement point under disturbance.

10^{-6} m/s^2/Hz$^{1/2}$, which means that the displacement drag-free controller can counteract the disturbance.

Considering the difference between the equivalent mass and the satellite mass, the same proportion of disturbance force is applied to the torsion pendulum, and the active disturbance force is

$$F_{\text{dis}} = 0.8 \sin(2\pi \cdot 0.05 \cdot t) + 4.1 \, \mu\text{N}. \tag{15}$$

Figure 21 shows the spectrum density of acceleration amplitude at the displacement measurement point of the torsion pendulum during the experiment, and its peak point is the response of the torsion pendulum under the disturbance force of equation (15). Compared with Fig. 19, the smaller disturbance force does not excite the frequency doubling response on the torsion pendulum.

In Fig. 22, the acceleration amplitude spectral density (as shown in the red curve in the figure) is obtained by numerical simulation at the measurement point under the disturbance force of equation (15). The peak value is the main frequency response under the disturbance force, and the secondary peak value is the response of the disturbance force on the system. Under the control of displacement without drag, the disturbance at the measuring point on the torsion pendulum is reduced from 10^{-6} m/s^2/Hz$^{1/2}$ to less than 10^{-7} m/s^2/Hz$^{1/2}$, and the disturbance suppression ability is better than 20 dB.
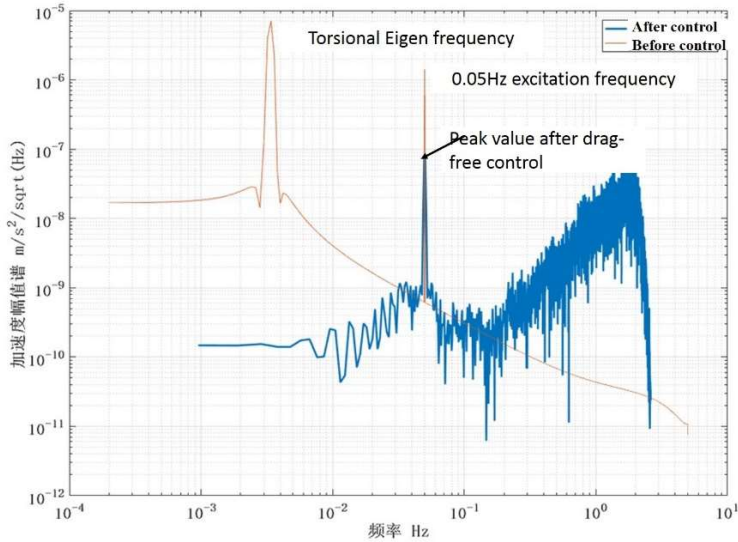
Fig. 22. Comparison of acceleration amplitude at measurement point of torsion pendulum before and after disturbance.

4. Conclusion

In this paper, the problem of ground hardware in the loop simulation for the drag-free control of Taiji-1 experimental satellite is studied. The experimental scheme of ground suspension torsion pendulum based on small angle approximation is proposed. Based on the principle of dynamic equivalence, the parameters of ground experiment model are designed. According to the experimental requirements, capacitive displacement sensor with nanometer resolution is selected as measurement sensor, and electrostatic comb is used to generate weak force instead of micro thrust system on satellite. On the basis of the above, the ground semi-physical simulation system is built, and the data acquisition and output control are realized by NI DAQ hardware and software. The ground displacement drag-free controller is designed. Through the ground experiment and simulation, it is found that the controller can stably control the torsion angle, and the residual acceleration at the measuring point can reach 10^{-9} m/s^2/Hz$^{1/2}$ in the measurement frequency band of 0.01~1 Hz. In order to suppress the motion of the torsion pendulum, a common mode suppression controller is designed. The simulation results show that the controller can effectively suppress the long-period simple pendulum motion. Finally, the anti-disturbance performance of the drag-free displacement controller under the disturbance force is verified. The experimental results show that the disturbance rejection performance of the controller is better than 20 dB at 0.05 Hz.

Acknowledgments

References

1. J. Leitner, Investigation of drag-free control technology for earth science constellation missions, NASA Earth Science Technology Office Final Study Report, Vol. 15 (2003).
2. J. A. Johannessen, G. Balmino, C. L. Provost *et al*., *Surveys Geophys.* **24**, 339 (2003).
3. C. W. F. Everitt *et al*., *Phys. Rev. Lett.* **106**, 221101 (2011).
4. P. Amaro-Seoane *et al*., *Class. Quantum Grav.* **29**, 124016 (2012).
5. F. Antonucci *et al*., *Class. Quantum Grav.* **28**, 094001 (2011).
6. E. Canuto, *Automatica* **44**, 1766 (2008).
7. U. Johann, F. Gath, W. Holota, H. Schulte and D. Weise, Novel payload architectures for LISA, in *Proc. 6th Int. LISA Symp.*, NASA Goddard Space Flight Center, Greenbelt, MD, 2006, pp. 304–311.
8. M. Armano *et al*., *Class. Quantum Grav.* **26**, 094001 (2009).
9. D. Gerardi, G. Allen, J. W. Conklin *et al*., *Rev. Sci. Instrum.* **85**, 011301 (2014).
10. D. Chapman, M. Zentgraf and R. Jafry, Drag-free control design including attitude transition for the STEP mission, in *Proc. 5th ESA Int. Conf. Spacecraft Guidance Navigation and Control*, European Space Agency, Noordwijk, The Netherlands, October 2002, pp. 551–557.
11. D. Bortoluzzi, M. Da Lio, R. Dolesi, W. Weber and S. Vitale, *Class. Quantum Grav.* **20**, S227 (2003).
12. W. Fichter, P. Gath, S. Vitale and D. Bortoluzzi, *Class. Quantum Grav.* **22**, S139 (2005).
13. S. F. Wu and D. Fertin, *Acta Astronautica* **62**, 668 (2008).
14. L. Pettazzi, A. Lanzon, S. Theil *et al*., *J. Guid. Control Dyn.* **32**, 1609 (2009).
15. D. B. Debra, J. C. Mathiesen, R. R. A. Va, *J. Spacecraft Rockets* **5**, 1040 (1968).
16. S. Kawamura, N. Kawashima and J. Hirao, Drag-free satellite simulator, the Institute of Space and Astronautical Science, Report No. 615, September 1984.
17. M. Bassan, A. Cavalleri, M. De Laurentis *et al*., *Phys. Rev. Lett.* **116**, 051104 (2016).
18. H. B. Tu, Y. Z. Bai, Z. B. Zhou *et al*., *Class. Quantum Grav.* **278087**, 205016 (2010).
19. Y. X. Yang, L. C. Tu, S. Q. Yang *et al*., *Rev. Sci. Instrum.* **83**, 153001 (2012).
20. Y. Tu, L. Zhao, Q. Liu *et al*., *Phys. Lett. A* **331**, 354 (2004).